Structural basis of a protein partner switch that regulates the general stress response of α-proteobacteria

Julien Herrou[a], Grant Rotskoff[a], Yun Luo[a], Benoît Roux[a], and Sean Crosson[a,b,1]

[a]Department of Biochemistry and Molecular Biology, and [b]Committee on Microbiology, University of Chicago, Chicago, IL 60637

Edited by Carol A. Gross, University of California, San Francisco, CA, and approved April 5, 2012 (received for review October 14, 2011)

α-Proteobacteria uniquely integrate features of two-component signal transduction (TCS) and alternative sigma factor (σ) regulation to control transcription in response to general stress. The core of this regulatory system is the PhyR protein, which contains a σ-like (SL) domain and a TCS receiver domain. Aspartyl phosphorylation of the PhyR receiver in response to stress signals promotes binding of the anti-σ factor, NepR, to PhyR-SL. This mechanism, whereby NepR switches binding between its cognate σ factor and phospho-PhyR (PhyR∼P), controls transcription of the general stress regulon. We have defined the structural basis of the PhyR∼P/NepR interaction in *Caulobacter crescentus* and characterized the effect of aspartyl phosphorylation on PhyR structure by molecular dynamics simulations. Our data support a model in which phosphorylation of the PhyR receiver domain promotes its dissociation from the PhyR-SL domain, which exposes the NepR binding site. A highly dynamic loop–helix region (α3-α4) of the PhyR-SL domain plays an important role in PhyR∼P binding to NepR in vitro, and in stress-dependent activation of transcription in vivo. This study provides a foundation for understanding the protein-protein interactions and protein structural dynamics that underpin general stress adaptation in a large and metabolically diverse clade of the bacterial kingdom.

Bacteria use a diverse set of regulatory proteins to control gene expression in response to a changing environment. Among these, two-component signaling (TCS) systems and alternative sigma factors (σ) constitute two major classes of transcriptional regulators (Fig. 1 *A* and *B*). The recent discovery of PhyR in the α-proteobacteria (1, 2) provides an example of the confluence of TCS and σ-dependent transcriptional regulation in a single polypeptide. PhyR contains an N-terminal σ-like (SL) domain and a C-terminal TCS receiver domain. Stress-dependent phosphorylation of PhyR indirectly activates transcription of stress-response genes (3) through a unique protein partner switching mechanism detailed below (Fig. 1*C*).

PhyR-SL has sequence similarity to the EcfG-family of alternative σ factors (4), which are known to function as general stress regulators in the α-proteobacteria (3, 5–7). However, regions σ_2 and σ_4 of PhyR-SL are missing key residues required for interaction with DNA and RNA polymerase (RNAP) (4). This is consistent with the discovery that PhyR does not function as a true σ factor but, rather, indirectly controls gene expression through its interaction with NepR (3), an anti-σ^{EcfG} protein (3, 4). Specifically, stress-dependent phosphorylation of the PhyR receiver domain is proposed to disrupt its interaction with the SL domain, thereby enabling PhyR-SL to bind NepR (3). Phospho-PhyR (PhyR∼P) thus functions as an anti–anti-σ factor (i.e., a NepR binding factor) that releases σ^{EcfG} to directly regulate transcription during stress (Fig. 1*C*). This regulatory model is conceptually similar to the partner switching systems controlling σ^B (8) and σ^F (9) of *Bacillus subtilis* and other species (10), though the underlying mechanisms differ.

The biochemical, biophysical, and structural underpinnings of PhyR-regulated transcription remain largely uncharacterized. However, a recent high-resolution crystal structure of *Caulobacter crescentus* PhyR (11) in its unphosphorylated state informs several testable hypotheses centering on the molecular mechanism of PhyR function. As described in other species (3, 6, 7, 12), phosphorylation of *C. crescentus* PhyR increases its apparent affinity for the anti-σ^{EcfG} factor, NepR (13). Genetic and biochemical data on *C. crescentus* PhyR (11, 13) support the aforementioned partner switching model (3), in which PhyR∼P/NepR complex formation during stress activates transcription of the general stress regulon through σ^{EcfG} (more commonly known as σ^T in *C. crescentus*).

In this study, we characterize the molecular and structural basis of PhyR function as an anti–anti-σ factor. A crystal structure of the SL domain of *C. crescentus* PhyR in complex with the anti-σ factor NepR is combined with molecular dynamics (MD) simulations, in vitro binding studies, and in vivo transcription assays to define the functional PhyR-NepR binding interface. NepR binds regions σ_2 and σ_4 of PhyR-SL across the same molecular surface occluded by the receiver domain in the unphosphorylated structure of PhyR. Thus, the receiver domain must undock from the SL domain before NepR binding. We further demonstrate that the dynamic α3-α4 loop–helix region of the PhyR-SL domain is required for high-affinity binding of PhyR∼P to NepR in vitro, and for activation of σ^T-dependent transcription in vivo. This study defines key molecular determinants of the PhyR/NepR/σ^{EcfG} protein partner switch that regulates the general stress response in the α-proteobacteria.

Results

Structure of the PhyR-SL/NepR Complex. The PhyR-SL domain is known to bind NepR constitutively when the C-terminal receiver domain is deleted (3). To characterize PhyR binding to NepR structurally, we first coexpressed and purified the isolated PhyR-SL domain ($\mathrm{PhyR}_{\Delta\mathrm{Rec}}$) bound to NepR. The crystal structure of *C. crescentus* $\mathrm{PhyR}_{\Delta\mathrm{Rec}}$ in complex with NepR carries a deletion of 13 amino acids (ΔG68-H80) in the α3-α4 loop (LΔ13), which increased protein stability and facilitated crystallization. Crystallographic data are summarized in Table 1. A simulated annealing composite omit map of a region of the $\mathrm{PhyR}_{\Delta\mathrm{Rec}}$(LΔ13)/NepR complex structure is presented in Fig. S1.

$\mathrm{PhyR}_{\Delta\mathrm{Rec}}$(LΔ13) (i.e., the PhyR-SL domain) and NepR form a heteromeric protein complex in the crystal (Fig. 2). In this structure, PhyR-SL is a homodimer. Regions σ_2 and σ_4 of each

---

Author contributions: J.H. and S.C. designed research; J.H., G.R., and Y.L. performed research; J.H. and S.C. contributed new reagents/analytic tools; J.H., G.R., Y.L., B.R., and S.C. analyzed data; and J.H., G.R., B.R., and S.C. wrote the paper.

The authors declare no conflict of interest.

This article is a PNAS Direct Submission.

Data deposition: The atomic coordinates and structure factors have been deposited in the Protein Data Bank, www.pdb.org (PDB ID code 3T0Y).

[1] To whom correspondence should be addressed. E-mail: scrosson@uchicago.edu.

See Author Summary on page 7973 (volume 109, number 21).

This article contains supporting information online at www.pnas.org/lookup/suppl/doi:10.1073/pnas.1116887109/-/DCSupplemental.

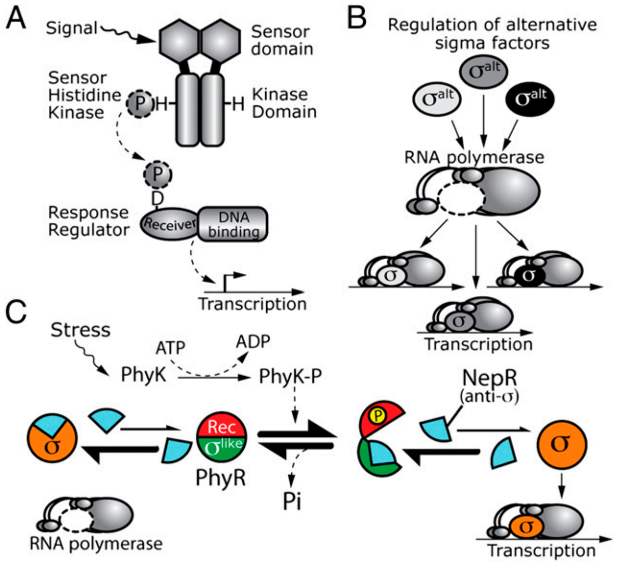

Fig. 1. PhyR regulatory system integrates features of TCS and alternative σ regulation. (*A*) Cartoon depicts transcriptional regulation by an archetypal TCS system. (*B*) Differential regulation of alternative σ factors under specific environmental conditions is a mechanism of transcriptional control. (*C*) Hybrid PhyR protein contains an N-terminal SL domain (green) and a C-terminal receiver (Rec) domain (red). σ^T (orange) is bound and inhibited by the anti-σ factor NepR (blue) under normal growth conditions. Phosphorylation of PhyR increases its affinity for NepR, which frees σ^T to bind RNAP and regulate transcription during stress.

PhyR-SL domain are separated about a flexible loop region (α3-α4) and swapped between two monomers; region σ_2 of molecule A (σ_2^A) dimerizes with region σ_4 of molecule B (σ_4^B), and vice versa. Consequently, each complex contains two copies of PhyR-SL that are organized as follows: σ_2^A σ_4^B and σ_2^B σ_4^A (Fig. 2). Gel filtration on purified PhyR-SL (either WT or the LΔ13 variant) at micromolar concentrations indicates that the SL domain alone likely exists as an open monomer in solution, with the elution volume suggesting an extended conformation. Addition of NepR to these proteins results in formation of the dimeric PhyR-SL/NepR complex (2:2 ratio) observed in the crystal (Fig. S2 *B* and *C*).

If we consider each swapped σ_2-σ_4 PhyR-SL dimer in the crystal as a single SL domain, each adopts a structure that is nearly identical (rmsd = 0.75 Å) to the closed SL domain reported in full-length PhyR [Protein Data Bank (PDB) ID code 3N0R] (11). We observe a bundle of seven α-helices with α1, α2, and α3 corresponding to region σ_2 and α5, α6, and α7 corresponding to region σ_4 (Fig. 3*B*). The major difference in the structure of the SL domain presented here compared with the full-length PhyR protein is the shifted position of helix α4. Specifically, α4 in the $\text{PhyR}_{\Delta\text{Rec}}$(LΔ13)/NepR complex occupies a position that more closely matches what has been reported in other region σ_4 structures, including *Thermatoga maritima* σ^A (14), *Mycobacterium tuberculosis* σ^C (15), *Escherichia coli* σ^E (16), and *M. tuberculosis* σ^L (17) (Fig. 5 *A* and *C*).

Because the PhyR-SL domain adopts a dimeric conformation in this structure, it was necessary to test whether full-length PhyR forms dimers in solution on phosphorylation. To do so, we conducted gel filtration and small-angle X-ray scattering (SAXS) experiments on full-length PhyR in the presence and absence of 25 mM acetyl phosphate (AcP), which has been reported to phosphorylate and activate *C. crescentus* PhyR (13). At a concentration of ~300 μM, full-length His-PhyR eluted at a volume consistent with a monomer from a Superdex 75 column (GE Healthcare) in the presence and absence of AcP (Fig. S2*A*). Additionally, the radii of gyration (R_g) determined by SAXS from 8-μM and 20-μM PhyR samples measured in the presence and absence of AcP,

Table 1. Crystallographic data and refinement statistics

Data collection statistics (SeMet)

Energy, keV	12.66						
Resolution range, Å	30-2.1 along b* and c*; 30-2.7 along a*						
Unique reflections	17,325						
R_{merge}[†]	0.07						
$\langle I\rangle/\langle\sigma_I\rangle$	28.2						
Redundancy	7.9						
Completeness	95.0%[†]						
Phasing statistics[‡] (D_{min}), Å							
	6.0	3.8	3.0	2.6	2.3	2.1	Overall
Figure of merit	0.45	0.46	0.32	0.22	0.17	0.13	0.27
Refinement statistics							
Space group	$C222_1$						
a, b, c; Å	75.3, 105.3, 97.9						
R_{cryst}[§]	20.0						
R_{free}[¶]	25.1						
$\langle B\rangle$, $Å^2$	36.7						
rmsd of bond lengths, Å	0.008						
rmsd of bond angles, °	1.16						
Ramachandran analysis							
Preferred, %	97						
Disallowed, %	<1						

D_{min}, the resolution limit of diffraction by the crystal.

[†] $R_{merge} = \Sigma_{hkl}\Sigma_i |I_i - \langle I\rangle|/\Sigma_{hkl}\Sigma_i I_i$, for all data greater than −3; completeness to 2.7 Å $\langle I\rangle/\langle\sigma_I\rangle$ greater than 2.

[‡] Experimental phases were determined by the Autosol SAD routine in PHENIX using the anomalous signal from selenium. Total figure of merit values are based on experimental phase information (prior) for all reflections.

[§] $R_{cryst} = \Sigma_{hkl}||F_{obs}| - |F_{calc}||/\Sigma_{hkl}|F_{obs}|$ using ellipsoidally truncated and anisotropically scaled reflections as described in *Materials and Methods*.

[¶] R_{free} uses 1,729 total reflections for cross-validation.

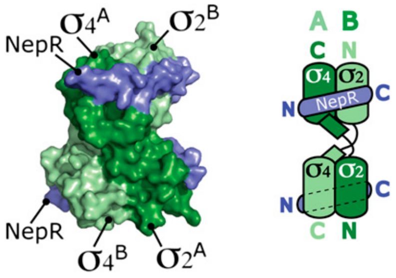

Fig. 2. Surface representation of the $\text{PhyR}_{\Delta\text{Rec}}$(LΔ13)/NepR dimer. Open $\text{PhyR}_{\Delta\text{Rec}}$(LΔ13) molecule A (light green) dimerizes with open $\text{PhyR}_{\Delta\text{Rec}}$(LΔ13) molecule B (dark green). Bound NepR is colored blue (PDB ID code 3T0Y).

respectively, were consistent with the expected monomeric R_g (Fig. S3). Thus, we conclude that full-length *C. crescentus* PhyR remains monomeric on phosphorylation.

Although the crystal structure presented here clearly shows that the isolated SL domain is capable of opening about the flexible α3-α4 loop region and forming a homodimer, its binding to NepR occurs in a closed conformation (Fig. 3*B*). Binding at a 1:1 ratio between PhyR and NepR is supported by gel filtration of the full-length *C. crescentus* His-PhyR~P/NepR protein complex (~300 μM), which elutes at a volume consistent with a 1:1 heterodimer (Fig. S2*A*). These data provide evidence for a full-length PhyR~P/NepR binding model in which NepR binds monomeric PhyR-SL in a closed conformation.

Defining the Anti-σ/Anti–Anti-σ Interaction. The anti-σ factor, NepR, contains 68 amino acids; electron density for the first 29 N-terminal residues and the last 6 residues of the C terminus is not visible in our maps. Despite low sequence conservation of these segments (Fig. 3*A*), we cannot exclude the possibility that the N- and C-terminal regions of NepR are involved in interaction with the receiver domain or with σ^T. The 33 NepR residues visible in the density maps constitute two α-helices connected by a short, four-residue linker (Fig. 3*A*). NepR wraps around regions σ_2 and σ_4 of the PhyR-SL domain (i.e., the anti–anti-σ domain) (Fig. 3*B*), occupying the same molecular surface of PhyR-SL in a nearly identical conformation on both copies in the asymmetric unit (rmsd = 0.44 Å). The portion of NepR that binds PhyR-SL constitutes the region of primary sequence that is most conserved among NepR orthologs from other α-proteobacteria (Fig. 3 *A* and *B*).

NepR and the receiver domain of PhyR bind the same surface of PhyR-SL (Figs. 3*C* and 4). Thus, we conclude that the receiver domain must undock from PhyR-SL on phosphorylation to reveal the NepR binding surface. A presentation of surface hydrophobicity, polarity, and conservation is presented in Fig. 4.

To validate our crystal structure functionally, we next tested whether key PhyR-SL/NepR interactions observed in the crystal are required for binding in solution, and for stress-dependent activation of transcription in *C. crescentus* cells. In the crystal structure, residues R15 and R16 of the PhyR-SL domain interact extensively with NepR (Fig. 3*D*). As such, we mutated both R15 and R16 to alanine and conducted a pull-down binding assay between maltose-binding protein (MBP)-NepR and His-$\text{PhyR}_{\Delta\text{Rec}}$(R15A-R16A); we could detect no interaction between these two proteins. The same experiment performed with MBP-NepR and WT His-$\text{PhyR}_{\Delta\text{Rec}}$ revealed a strong binding interaction (Fig. 6*A*). Replacement of WT *phyR* with these mutant *phyR* alleles on the *C. crescentus* chromosome showed that both *phyR(R15A-R16A)* and *$\text{phyR}_{\Delta\text{Rec}}$(R15A-R16A)* are stably expressed but are nonfunctional as assayed by transcription from a σ^T-dependent reporter (Fig. 6*A*). Thus, the interactions observed in the crystal between NepR and PhyR residues R15 and R16 are necessary for PhyR function as an anti–anti-σ factor.

Structural Dynamics of the PhyR Anti–Anti-σ Factor. Structures presented previously (11) and herein suggest a model in which conformational changes at the PhyR-SL/receiver domain interface and in the α3-α4 region of the PhyR-SL domain have a role in PhyR function as an anti–anti-σ factor. To assess the dynamics of full-length PhyR, we performed an atomistic MD simulation to 320 ns in a fully explicit, solvated system. This simulation used the high-resolution (1.25 Å) crystal structure of full-length PhyR (PDB ID code 3N0R) phosphorylated at resi-

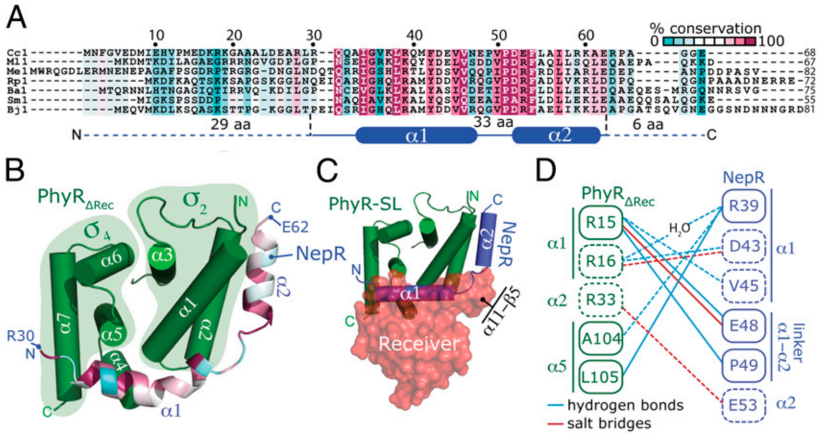

Fig. 3. Structure of the $\text{PhyR}_{\Delta\text{Rec}}$(LΔ13)/NepR complex (PDB ID code 3T0Y) (*A*) Amino acid sequence alignment of *C. crescentus* (Cc) NepR with orthologous sequences from other α-proteobacteria (Me, *M. extorquens*; Bj, *Bradyrhizobium japonicum* USDA110B; Rp, *Rhodopseudomonas palustris* CGA009; ML, *Mesorhizobium loti* MAFF303099; SM, *Sinorhizobium meliloti* 1021; and Ba, *Brucella abortus* 2308). Residues are highlighted according to degree of conservation (upper right key). The regions of NepR sequence not visible in the electron density maps are marked (dashed line) below the alignment. (*B*) Ribbon structure of the $\text{PhyR}_{\Delta\text{Rec}}$(LΔ13)/NepR complex. Residues of NepR are colored by sequence conservation (upper right key). PhyR-SL regions σ_2 and σ_4 are outlined in green, and NepR residues for which there was visible electron density (R30 to E62) are marked. (*C*) Structural alignment between the full-length PhyR (PDB ID code 3N0R) and the $\text{PhyR}_{\Delta\text{Rec}}$(LΔ13)/NepR structures reveals overlap between the PhyR receiver domain (red) and the NepR (blue) interaction surfaces. (*D*) Residue interaction map (<3.5 Å) between NepR (blue) and $\text{PhyR}_{\Delta\text{Rec}}$(LΔ13) (green). Hydrogen bonds (blue lines) and salt bridges (brown lines) are shown. Dashed lines correspond to interactions that are present in only one of the $\text{PhyR}_{\Delta\text{Rec}}$(LΔ13)/NepR complexes in the asymmetric unit. Residues are numbered, and their locations in the different helices are annotated.

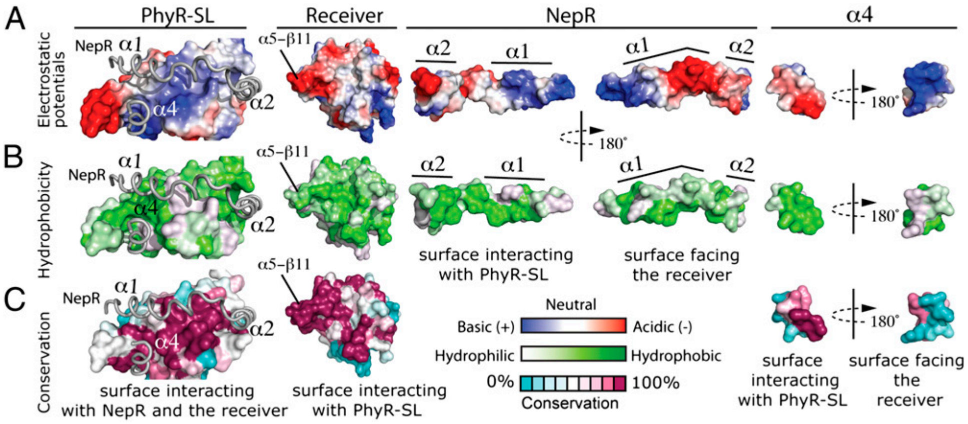

Fig. 4. Electrostatic (*A*), hydrophobic (*B*), and surface conservation (*C*) maps of the different interaction surfaces of the PhyR$_{\Delta\mathrm{Rec}}$(LΔ13) domain, the PhyR receiver domain, NepR, and helix α4.

due D192 as a starting model. We observed significant structural change in two key regions: (*i*) the loop between α-helix 11 and β-strand 5 of the receiver domain and (*ii*) the α3-α4 loop and helix α4 of the PhyR-SL domain (Fig. 5*B*, heat maps are presented in Fig. S4).

The molecular surface of the receiver domain in which we observe the largest conformational change in our simulation, the α11-β5 loop, is highly conserved and directly contacts the PhyR-SL domain (Figs. 3*C*, 4, and 5 *A* and *B*). This is a region of structure that is known to undergo conformational change on phosphorylation in multiple two-component receiver proteins (18–22). We observe that retraction of the α11-β5 loop from PhyR-SL begins at ∼120 ns, which allows solvent access to the PhyR receiver/SL interface (Fig. 5*B* and Movie S1).

Within the PhyR-SL domain, the regions of the α3-α4 loop and helix α4 are highly dynamic regions of structure (Fig. 5*B*). Indeed, among all the regions of PhyR, the α3-α4 loop and α4 have the highest crystallographic B-factors (11) and exhibit the largest structural shifts in our MD simulation. The hydrophobic and highly conserved face of this amphipathic helix (Fig. 4 *B* and *C*) is loosely docked against helices α1 and α3 of region σ_2 in the full-length PhyR structure. This same conserved helical face is in a different conformation in the PhyR-SL/NepR complex, where it is docked against helices α1 and α5 (Fig. 5*A*). This position of α4 in the complex structure is equivalent to what has been reported for orthologous α4 amphipathic helices of classic σ factors (Fig. 5*C*).

Highly Dynamic α3-α4 Region of PhyR Is Required for Stress-Dependent Regulation of Transcription. Expression of the isolated PhyR-SL domain (PhyR$_{\Delta\mathrm{Rec}}$) is known to sequester NepR, and thus constitutively derepress transcription of the general stress regulon in *Methylobacterium extorquens* (3). We have confirmed this result in *C. crescentus*; chromosomal replacement of WT *phyR* with the *phyR*$_{\Delta Rec}$ allele produces stable protein that consititutively up-regulates transcription from a σ^{T}-dependent reporter (Fig. 6*A*). Using σ^{T}-dependent transcription as a proxy for PhyR-SL/NepR interaction in vivo, we attempted to assess the functional role of the dynamic α3-α4 region in NepR interaction. However, *phyR*$_{\Delta Rec}$ alleles in which we truncated the α3-α4 coding sequence failed to produce stable protein in *C. crescentus* (Fig. S5), precluding functional analysis.

We next tested α3-α4 function in the context of full-length PhyR. We generated a set of *C. crescentus phyR* allelic replacement strains in which the α3-α4 loop and α4 coding sequence were removed (Fig. 6*B*). All these PhyR loop mutants produced soluble and stable protein in vivo (Fig. 6*C*). Deletion of the first five amino acids of the α3-α4 loop (LΔ5 = ΔQ70-G74) modestly reduced (∼20%) stress-dependent transcriptional ac-

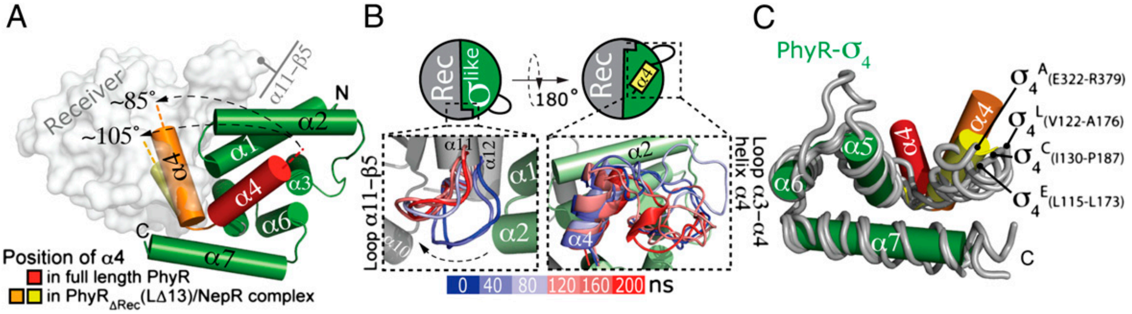

Fig. 5. Molecular dynamics simulation of PhyR∼P and structural analysis of helix α4 position. (*A*) Surface model of the PhyR receiver domain (white) interacting with the SL domain (green cylinders). The position of helix α4 in the unphosphorylated full-length PhyR structure (PDB ID code 3N0R) is shown in red; the position(s) of helix α4 in the PhyR$_{\Delta\mathrm{Rec}}$(LΔ13)/NepR complex are shown in orange and yellow (PDB ID code 3T0Y). (*B*) Conformational change of the α11-β5 receiver loop and the α3-α4 region of PhyR between 0 ns (blue) and 200 ns (red). The receiver (Rec) domain (gray) and SL domain (green) are shown (corresponding heat maps are provided in Fig. S4). (*C*) Superposition of region σ_4 of the PhyR-SL domain (green) with the structures of region σ_4 of σ^{A} (*T. maritime*, PDB ID code 1TTY), σ^{C} (*M. tuberculosis*, PDB ID code 2O8X), σ^{E} (*E. coli*, PDB ID code 1OR7), and σ^{L} (*M. tuberculosis*, PDB ID code 3HUG) (all in gray coils; the first and last residues of each structure are labeled). The position of helix α4 in the full-length PhyR structure (PDB ID code 3N0R) is rendered as a red cylinder. Two positions of helix α4 in the two PhyRΔRec(LΔ13)/NepR complexes in the asymmetric unit are shown as yellow and orange cylinders (PDB ID code 3T0Y).

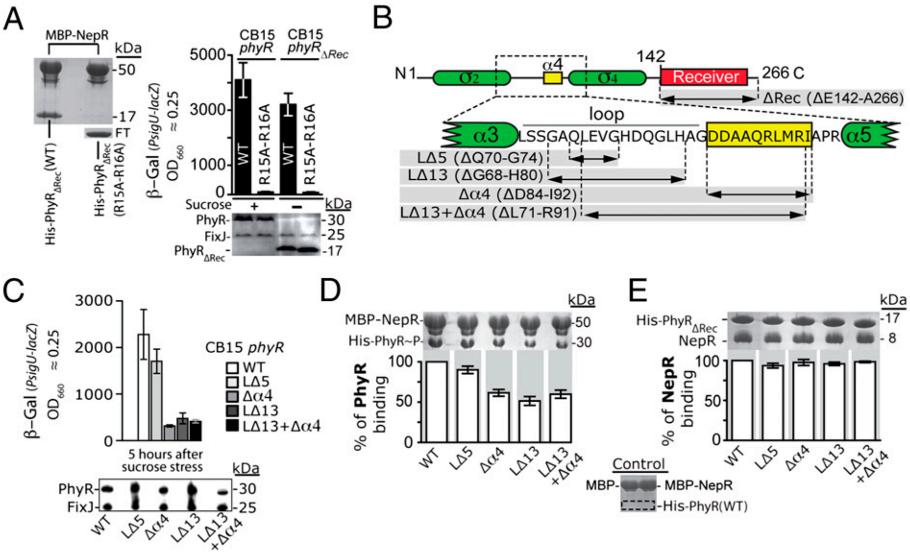

Fig. 6. (*A*) Testing the effect of R15A-R16A mutations in PhyR-SL. (*Left*) Pull-down binding assay between MBP-NepR and His-PhyR$_{\Delta Rec}$(WT) (lane 1) or His-PhyR$_{\Delta Rec}$(R15A-R16A) [lane 2; unbound protein was present in the column flow-through (FT)]. (*Right*) Transcription (with or without osmotic stress) from a σ^T transcriptional reporter (P*sigU-lacZ*) in *phyR(R15A-R16A)* and *phyR$_{\Delta Rec}$(R15A-R16A)* strains. A Western blot measuring in vivo stability of these mutant proteins is shown below the bar graph; FixJ is the loading control. (*B*) Testing the functional role of PhyR region α3-α4 in the *C. crescentus* transcriptional response to osmotic stress. Boundaries of the engineered α3-α4 loop (LΔ) and helix α4 (Δα4) PhyR mutants used for functional and binding studies are shown. (*C*) Stress-regulated transcription from P*sigU-lacZ* in WT and the *phyR* mutant backgrounds depicted in *B* (LΔ5, LΔ13, LΔ13 + α4, and Δα4). In vivo stability of mutant PhyR proteins as determined by Western blotting is shown below the bar graph; FixJ is the loading control. (*D*) Pull-down binding assay of His-PhyR(WT) and His-PhyR α3-α4 loop mutants to MBP-NepR in the presence of AcP; quantification of eluted fractions resolved on SDS/PAGE gel is shown below the gel image. A control binding assay conducted in the absence of AcP is shown on the right. (*E*) Pull-down binding assay of His-PhyR$_{\Delta Rec}$ α3-α4 loop mutants to NepR. Quantification of eluted fractions resolved on SDS/PAGE gel is shown below the gel image. All experiments were conducted in triplicate. Mean values ± SEM are shown.

tivation from a σ^T-dependent reporter. A larger deletion of this loop (LΔ13 = ΔG68-H80) strongly attenuated (~80%) transcription under sucrose stress. Deletion of the entire loop plus α4 (LΔ13 + Δα4 = ΔL71-R91) or deletion of α4 alone (Δα4 = ΔD84-I92) showed equivalent attenuation of stress-regulated transcription (Fig. 6*C*). From these data, we conclude that the full α3-α4 loop and helix α4 are required for PhyR to function as an anti–anti-σ^T regulator during stress in vivo.

Intact α3-α4 Region Is Required for NepR Binding to Full-Length PhyR~P but Not to PhyR$_{\Delta Rec}$. We next sought to test whether the transcriptional deficiencies of α3-α4 PhyR mutants were a result of a defect in PhyR~P binding to NepR. Congruent with our observations in the transcription assays described above, a short loop deletion (LΔ5) did not significantly perturb binding of His-PhyR~P to MBP-NepR in a column pull-down assay. However, deletion of the entire α3-α4 loop (LΔ13), the loop plus α4 (LΔ13 + Δα4), or α4 alone (Δα4) decreased NepR binding by 45–65% under the tested protein concentrations and buffer conditions (Fig. 6*D* and *Materials and Methods*). Surprisingly, although an intact α3-α4 region was required for full binding of PhyR~P to MBP-NepR, we observed no differences in binding between MBP-NepR and His-PhyR$_{\Delta Rec}$ or any of the α3-α4 mutant variants of His-PhyR$_{\Delta Rec}$ (Fig. 6*E*). This provides evidence that the dynamic α3-α4 region is not required for high-affinity binding of isolated PhyR-SL to NepR. Rather, an intact α3-α4 region is an important determinant of NepR binding to PhyR-SL only when the PhyR receiver domain is present.

Association and Dissociation Kinetics of the PhyR~P/NepR Binding Interaction. Using surface plasmon resonance (SPR), we quantified the association (K_a) and dissociation (K_d) rate constants of full-length His-PhyR binding to MBP-NepR in the presence and absence of the phosphoryl donor, AcP. In the absence of AcP, we observed no binding between immobilized WT His-PhyR and MBP-NepR (across an MBP-NepR concentration range of 250 nM to 2 μM) (Fig. S6*F*). The addition of AcP to the flow buffer resulted in monophasic binding of MBP-NepR to immobilized His-PhyR(WT), with a calculated equilibrium affinity of 641 ± 92 nM (Table 2 and Fig. S6*A*). A WT PhyR mutant in which the receiver domain was deleted (His-PhyR$_{\Delta Rec}$) bound MBP-NepR with biphasic kinetics. However, the amplitude of the slow phase was minor (~10–20%). We attribute this slow phase to a minority of PhyR$_{\Delta Rec}$ dimers (which contain 2 His tags) interacting in a nonuniform way with the Ni^{2+} surface of the SPR chip. The major (fast) association and dissociation rates are comparable to WT His-PhyR binding to MBP-NepR. Specifically, we calculated that His-PhyR$_{\Delta Rec}$(WT) binds MBP-NepR with ~5.5-fold higher affinity (117 ± 18 nM) than His-PhyR~P. This difference in equilibrium affinity is almost entirely determined by a faster association rate constant (Table 2 and Fig. S6*C*).

In accordance with the pull-down assays described above, complete deletion of the α3-α4 loop and helix α4 does not significantly affect the association and dissociation rate constants of MBP-NepR binding to isolated PhyR-SL [His-PhyR$_{\Delta Rec}$(LΔ13 + Δα4)] (Table 2 and Fig. S6*D*). However, the identical α3-α4/helix α4 deletion in full-length PhyR [His-PhyR(LΔ13 + Δα4)] dramatically decreases the affinity of its interaction with MBP-NepR

Table 2. K_a **and** K_d **and calculated equilibrium affinities (**K_D**) of PhyR/NepR binding**

MBP-NepR binding to	K_a, (1/M·s) × 10^5	K_d, (1/s) × 10^{-1}	K_D, nM
His-PhyR(WT)~P	1.6 ± 0.1	1.1 ± 0.1	641 ± 92.6
His-PhyR(LΔ13 + Δα4)~P	ND*	ND	ND
His-PhyR$_{\Delta Rec}$(WT)	8.0 ± 1.0	0.9 ± 0.1	117 ± 18.0
His-PhyR$_{\Delta Rec}$(LΔ13 + Δα4)	11.5 ± 1.0	2.2 ± 0.8	193 ± 55.6

*Binding parameters could not be determined (ND) at the assessed concentrations.

in the presence of AcP. Although we observed very weak binding at the highest MBP-NepR concentration tested (2 μM), we were not able to determine a binding affinity from these data (Table 2 and Fig. S6*B*), because concentrations of MBP-NepR beyond 2 μM resulted in strong nonspecific binding to the SPR chip. These kinetic binding data provide additional evidence that the α3-α4 region of the PhyR-SL domain is required for efficient NepR binding to the full-length PhyR protein but not to the PhyR-SL domain alone.

Discussion

PhyR Dynamics and NepR Binding. We have defined the molecular basis of binding between the SL domain of PhyR and the anti-σ factor, NepR. In its unphosphorylated state, the PhyR receiver domain occludes the NepR binding site on PhyR-SL (Fig. 3*C*). Structural and biochemical data and MD simulations provide support for a model in which phosphorylation of the PhyR receiver domain results in opening of the PhyR structure (i.e., dissociation of the receiver domain from the SL domain), exposing the NepR binding site on PhyR-SL. MD provides evidence that the α11-β5 region of the receiver domain may have a latch-like function, stabilizing the PhyR receiver/SL interaction in the unphosphorylated state. The α11-β5 fully retracts from contact with the PhyR-SL domain by 200 ns in our simulation, consistent with a model in which PhyR∼P is switching from a closed state to an open state. The result, that α11-β5 undergoes the largest conformational change in the receiver domain in our simulation, agrees with our initial hypothesis (11) that this region plays a key structural role in conformational switching. Concomitant with retraction of α11-β5, we observe that several water molecules infiltrate the binding interface between the PhyR receiver domain and PhyR-SL (Movie S1).

An analysis of different σ/anti-σ complex structures in the Protein Data Bank (PDB) reveals that interaction between a σ factor and its cognate anti-σ factor can occur in a number of different ways (23–25). A flexible linker between regions σ_2 and σ_4 has been described as important for anti-σ interaction but also as a general structural feature required for proper association of σ with RNAP and with -10 and -35 sequences in the promoter (16, 26–29). In the case of PhyR, the SL domain is missing critical sequence required for it to function as a bona fide σ factor (4) yet retains the flexible loop (α3-α4) between regions σ_2 and σ_4. Based on the full-length, unphosphorylated structure of PhyR, we initially proposed (11) that PhyR-SL would open about the α3-α4 loop and that NepR would bind between regions σ_2 and σ_4, much like σ^E and RseA (16). The structure of the complex reported here shows that although regions σ_2 and σ_4 of PhyR-SL are capable of separating about the flexible loop, PhyR-SL binds NepR in a closed conformation. However, we cannot exclude the possibility that opening of regions σ_2 and σ_4 is in some way important for the PhyR-SL/NepR binding process.

Binding Competition Between NepR and the PhyR Receiver Domain. NepR and the PhyR receiver domain compete for the same binding surface on PhyR-SL. Thus, for this stress regulatory system to function properly, NepR must overcome binding competition from a high local concentration of receiver domain. Even when PhyR is phosphorylated, it is reasonable to presume that NepR must contend with some degree of receiver binding competition. We have presented both functional genetic and biochemical data that support a model in which the dynamic α3-α4 region of PhyR-SL is required for stable binding between PhyR∼P and NepR. We propose that the α3-α4 linker loop may function to reduce interaction between PhyR-SL and the phosphorylated PhyR receiver domain when PhyR is in its "active" form (i.e., when the PhyR receiver domain is not bound to PhyR-SL). The length of the α3-α4 loop is clearly important in controlling the affinity of NepR for full-length PhyR∼P and for activation of σ^T-dependent transcription. Although a short (5 residues) truncation of the loop is tolerated, excision of longer pieces of α3-α4 reduces PhyR∼P binding to NepR and attenuates transcriptional activation on stress insult. These results suggest that a conformational rearrangement requiring the long, dynamic α3-α4 loop is important for regulated binding between PhyR∼P and NepR.

α4 is directly tethered to the α3-α4 loop and is the most inherently dynamic region of secondary structure in PhyR, exhibiting substantial conformational change in our simulations at early time points (Movie S1). This provides evidence that α4 is held in a relatively high-energy configuration within the full-length, unphosphorylated PhyR structure. In the context of the PhyR-SL/NepR complex, α4 occupies an entirely different position, where it is packed against the PhyR-SL surface that interacts with the receiver domain. This structural orientation of α4 more closely resembles what has been reported in other σ structures (Fig. 5*C*). PhyR phosphorylation, and subsequent disruption of the SL/receiver interface, may free α4 to shift to this position. We propose that this configuration of α4 would stabilize the PhyR∼P/NepR complex by obstructing the receiver domain from interacting with PhyR-SL (Fig. 7).

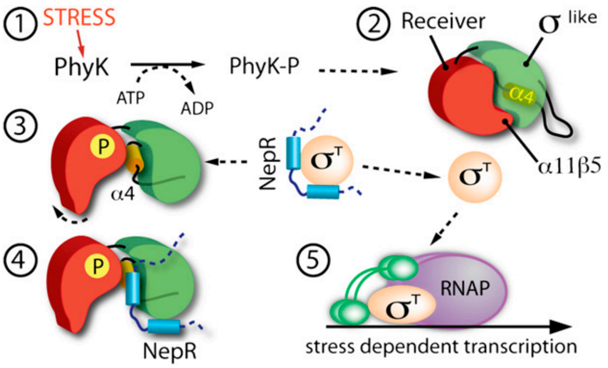

Fig. 7. Molecular model of regulated PhyR-NepR binding and σ-dependent transcription in *C. crescentus*. Under stress conditions a phosphoryl group on PhyK histidine kinase is transferred to the receiver domain (red) of PhyR, inducing structural changes that are transduced to a surface interaction loop (α11-β5) between the receiver domain and the SL domain (green) (1 and 2). Destabilization of the PhyR receiver/SL interface reveals the NepR binding surface; the dynamic α3-α4 loop and helix α4 (yellow) undergo a conformational change that helps to stabilize PhyR in the open state (3). In this open conformation, the PhyR-SL domain is able to bind NepR (blue) stably (4). σ^T (peach) is subsequently freed to bind RNAP (purple) and activate transcription of stress response genes (5).

Materials and Methods

Production of Recombinant PhyR Proteins. Heterologous expression of WT and mutant variants of *C. crescentus* PhyR and NepR was carried out in *E. coli* Rosetta (DE3) pLysS (Novagen). Protein was expressed from genes cloned into pET28c (Novagen), pETDuet-1 (Novagen), or pMALc2g (New England Biolabs) (strain, plasmid, and primer information is provided in Tables S1 and S2). Three classes of expression strains were obtained: pETDuet-1 strains coexpressing His-tagged PhyR or $\mathrm{PhyR}_{\Delta\mathrm{Rec}}$ with the NepR protein (growth in LB + ampicillin, 100 μg/mL), pET28c strains overexpressing His-tagged PhyR or $\mathrm{PhyR}_{\Delta\mathrm{Rec}}$ alone (growth in LB + kanamycin, 50 μg/mL), and a pMALc2g strain expressing an MBP-NepR fusion protein (growth in LB + ampicillin, 100 μg/mL).

Protein Expression and Purification. Liquid cultures for expression of recombinant WT and mutant PhyR and NepR were induced at an OD_{660} of 0.8 (37 °C, 220 rpm) by adding 1 mM isopropyl β-D-1-thiogalactopyranoside (IPTG; Gold Biotechnology). After 3 h, cells were harvested by centrifugation at 8,000 rpm for 20 min at 4 °C. Cell pellets were resuspended in 10 mM Tris·HCl (pH 7.4), 150 mM NaCl, and 10 mM imidazole (Fisher Scientific) with 5 μg/mL DNase I and 80 μg/mL PMSF (Sigma–Aldrich), and disrupted by two passages in a French pressure cell; the cell debris was removed by centrifugation at 14,000 rpm for 20 min at 4 °C.

For protein purified by nickel affinity chromatography (GE Healthcare), after loading the clarified lysate on a preequilibrated column, three washing steps were performed using 10 mM, 30 mM, and 75 mM imidazole Tris·NaCl buffers followed by elution with 500 mM imidazole Tris·NaCl buffer. The protein solution was then dialyzed against 10 mM Tris·HCl (pH 7.4) and 150 mM NaCl buffer to remove imidazole.

For purification of MBP-NepR fusion protein, an amylose resin column (New England Biolabs) was first equilibrated with 20 mM Tris (pH 7.4) and 200 mM NaCl. Cell lysate was loaded and washed five times with three column volumes of equilibration buffer. Protein was eluted with equilibration buffer supplemented with 10 mM maltose.

When necessary, purified proteins were concentrated using a centrifugal filter [3 kDa molecular weight cutoff (MWCO); Amicon–Millipore]. All purification steps were carried out at 4 °C. The protein purity was assessed by resolving the different fractions by 14% (wt/vol) SDS/PAGE gels.

Crystallization of the PhyR$_{\Delta Rec}$(LΔ13)/NepR Complex. Multiple attempts to crystallize NepR complexed with the WT SL domain of PhyR failed. We postulated that the disordered α3-α4 loop in the SL domain might perturb crystal packing. As such, we coexpressed NepR with a mutant of the PhyR-SL domain that is missing residues 68–80 [PhyR$_{\Delta Rec}$(LΔ13)]; these residues have been defined previously as the disordered α3-α4 loop in the full-length PhyR structure (11). Protein was expressed and purified as described above. All crystallization attempts were carried out using the hanging-drop, vapor-diffusion technique. The protein concentration was 30 mg/mL. Initial crystallization screening was carried out in 96-well microplates (Nunc). Trays were set using a Mosquito robot (TTP LabTech) and commercial crystallization kits (Nextal–Qiagen). The drops were set up by mixing equal volumes (0.1 mL) of the protein and the precipitant solutions equilibrated against 75 mL of the precipitant solution. After manual refinement (in 24-well plates; Hampton Research), the best crystals were obtained at 14 °C with the following crystallization solution: 100 mM 2-(N-morpholino)ethanesulfonic acid (MES) (pH 6.0), 20% PEG 2000 MME, and 200 mM NaCl. The drops were set up by mixing 4 μL of protein and 1 μL of the precipitant solutions equilibrated against 500 μL of precipitant. Crystals grew to their final size in 10 to 15 d and were soaked for 1 min in a precipitant solution containing 5 mM β-mercaptoethanol and 20% glycerol (Fisher) as a cryoprotectant before flash-freezing in a cryoloop (Hampton Research) (30). To produce selenomethionine (SeMet; Sigma–Aldrich) protein for experimental phase determination, proteins were expressed in defined medium as previously described (31).

Crystallographic Data Collection and Processing. Crystal diffraction data were collected at a temperature of 100 K on beamline 21-ID-D (Life Sciences Collaborative Access Team, Advanced Photon Source) using a MAR Mosaic 300 detector and an oscillation range of 1°. Diffraction images were reduced using the HKL 2000 suite (32). Diffraction data revealed that the crystals belonged to the orthorhombic space group C222$_1$, with cell dimensions a = 75.4 Å, b = 105.3 Å, and c = 97.9 Å. Diffraction from these crystals was moderately anisotropic (D_{min} = 2.1 Å along b* and c* and 2.7 Å along a*, where Dmin is the diffraction limit of the crystal). The reflection set was ellipsoidally truncated and anisotropically scaled before refinement using the method of Strong and colleagues (33).

Phasing and Refinement. Diffraction from a single native crystal of the PhyR$_{\Delta Rec}$(LΔ13)/NepR protein complex containing SeMet was measured at an energy of 12.66 keV (0.979 Å) and phased by single-wavelength anomalous dispersion (34). Six selenium sites were located within the asymmetric unit using the Autosol SAD routine in PHENIX (35). Two PhyR$_{\Delta Rec}$(LΔ13)/NepR complexes were present per asymmetric unit. The initial PhyR$_{\Delta Rec}$(LΔ13)/NepR structure was built de novo from these experimental maps using the PHENIX AutoBuild routine. Manual model building, solvent addition, and refinement of this initial structure were conducted iteratively using Coot (36) and phenix.refine (Table 1). The structure was refined to a final R_{cryst} of 20.0% and R_{free} of 25.1%; the Rcryst and Rfree residuals are defined in the legend of Table 1. Coordinates of *C. crescentus* PhyR$_{\Delta Rec}$(LΔ13)/NepR have been deposited in the Protein Data Bank (PDB ID code 3T0Y).

Gel Filtration Chromatography. Protein oligomeric state was assessed using gel filtration chromatography. Three hundred microliters of purified His-PhyR (WT) (10 mg/mL, ∼300 μM), His-PhyR(WT)/NepR (10 mg/mL, ∼300 μM; purification steps carried out in the presence of 25 mM AcP and 5 mM Mg^{2+}), His-PhyR$_{\Delta Rec}$(WT)/NepR (5 mg/mL, ∼100 μM), and His-PhyR$_{\Delta Rec}$(LΔ13)/NepR (5 mg/mL, ∼100 μM) complexes was loaded onto a Superdex 75 HR 10/30 gel filtration column (GE Healthcare). Running buffer was 10 mM Tris (pH 7.4) and 150 mM NaCl. Buffer to measure elution volume of PhyR(WT)∼P protein and PhyR(WT)∼P/NepR complex was supplemented with 25 mM AcP and 5 mM $MgCl_2$, which has previously been reported to catalyze phosphorylation of *C. crescentus* PhyR (13). Gel filtration experiments were also carried out on purified His-PhyR$_{\Delta Rec}$(WT) and His-PhyR$_{\Delta Rec}$(LΔ13) proteins in the absence of bound NepR. Because these truncated variants of PhyR were unstable during the concentration steps and gel filtration, 10 mM Tris (pH 7.4) and 150 mM NaCl buffer was supplemented with 200 mM imidazole, which improved solubility. Three hundred microliters of each recombinant protein (10 mg/mL, ∼600 μM) was loaded on the gel filtration column. The protein composition of the column fractions was assessed by 14% SDS/PAGE gel.

SAXS. SAXS data were collected at Advanced Photon Source beamline 18-ID (Biophysics Collaborative Access Team). Unphosphorylated PhyR in 10 mM Tris (pH 7.5) and 150 mM NaCl was suspended in a 1-mm capillary at a final concentration of ∼20 μM, and SAXS was measured from this sample. Scattering from PhyR under phosphorylating conditions [10 mM Tris (pH 7.5), 150 mM NaCl, 5 mM $MgCl_2$, 25 mM AcP) was measured at a final concentration of ∼8 μM. Scattering data were recorded on an Aviex CCD detector, and data analysis was conducted using a custom SAXS analysis plug-in implemented in Igor Pro (WaveMetrics).

Engineering Allelic Replacement Strains. *C. crescentus* CB15 strains in which the WT *phyR* allele was replaced with different *phyR* mutant alleles were built using a double-recombination gene replacement strategy (37). pNPTS138 carries the *npt*I gene to select for single integrants on kanamycin and the *sac*B gene for counterselection on sucrose. Transformation of *C. crescentus* and sucrose counterselection for allelic replacement were carried out as described previously (38). PCR and Sanger sequencing of the PCR product confirmed allele replacement. Primer, plasmid, and strain information is provided in Tables S1 and S2.

Stress Response Transcriptional Assays. It is known that transcription of *sigU* is up-regulated by the general stress σ factor σ^T on osmotic or oxidative stress insult (5). The plasmid pRKLac290-P*sigU*, which contains the *sigU* promoter transcriptionally fused to *lacZ*, was conjugated into WT *C. crescentus* CB15 and strains in which the WT *phyR* allele was replaced with full-length *phyR* variants (R15A-R16A, LΔ5, LΔ13, LΔ13 + $\Delta\alpha$4, and $\Delta\alpha$4) and *phyR*$_{\Delta Rec}$ variants (WT, R15A-R16A, LΔ5, LΔ13, LΔ13 + $\Delta\alpha$4, and $\Delta\alpha$4). Each mutant was evaluated for its ability to activate transcription from the P*sigU*-*lacZ* reporter fusion.

All strains were grown in peptone/yeast extract (PYE) medium (+1 μg/mL tetracycline) at a starting OD_{660} of 0.05 (30 °C, 220 rpm) and stressed by adding 150 mM sucrose to the culture medium (5) at the beginning of the experiment. At $OD_{660} \approx 0.25$, β-galactosidase activities were measured in triplicate as previously described (39). Stability of mutant proteins was assessed by Western blot analysis.

Western Blot Analysis of WT and Mutant PhyR Proteins. The effect of deleting different *phyR* regions (receiver domain, loop, and α4) on PhyR protein stability was assessed by Western blot analysis. *phyR* and mutant variants thereof were cloned into pMT585 (40) containing the sequence for a human influenza HA epitope tag at the 5′ end of the multiple cloning site. Inserts were obtained by NdeI/EcoRI digestion of pCR-BLUNT II-TOPO plasmids (Invitrogen) carrying the different versions of *phyR* and directly ligated in pMT585-HA plasmid. These clones yielded xylose-inducible, N-terminal HA protein fusions (primers, plasmid, and strain information is provided in Tables S1 and S2). The different pMT585-HA-*phyR* fusion plasmids were conjugated into a *C. crescentus* CB15 Δ*phyR* background from an *E. coli* TOP10 donor strain.

Western blots were performed as follows. After 5 h of induction with 0.15% D-xylose (Fisher) (30 °C, shaken at 220 rpm, initial OD_{660} = 0.05, final OD_{660} = 0.5), 50 mL of PYE (+5 μg/mL kanamycin) culture was pelleted (8,000 rpm for 10 min) and resuspended in 1.5 mL of 10 mM Tris (pH 7.4) and 150 mM NaCl buffer. Each sample was French-pressed and centrifuged at 14,000 rpm for 20 min to remove cell debris. Ten microliters of supernatant was mixed with 3 μL of SDS loading buffer, incubated at 95 °C for 5 min, resolved on a 14% SDS/PAGE gel, and blotted onto a 0.2-μM PVDF membrane (Millipore). Blotting and antibody incubation were performed as previously described (38). Briefly, after transfer and blocking steps, the membrane was incubated with a mix of mouse monoclonal anti-HA (Sigma–Aldrich) and rabbit polyclonal anti-FixJ (loading control) primary antibodies. Anti-mouse and anti-rabbit HRP secondary antibodies (ThermoFisher Scientific) were used for detection. Western blots were developed with SuperSignal West Femto chemiluminescent substrate (ThermoFisher Scientific).

PhyR/NepR Copurification/Pull-Down Assays. MBP-NepR from the clarified lysate of a 50-mL culture pellet (*Protein Expression and Purification*) was bound to 600 μL of amylose resin. A 50-mL wash of the beads was performed with 20 mM Tris (pH 7.4) and 200 mM NaCl buffer. One hundred microliters of MBP-NepR beads was mixed with 500 μL of His-PhyR(WT) purified protein (concentration of ∼50 μM). This same protocol was applied to the His-PhyR "loop" mutant proteins [PhyR(LΔ5), PhyR(Δα4), PhyR(LΔ13), and PhyR(LΔ13 + Δα4)]. In each sample, 1 mL of 20 mM Tris (pH 7.4) and 200 mM NaCl buffer supplemented with 5 mM MgCl$_2$ and 25 mM AcP was added to induce phosphorylation of PhyR. After 1 h of incubation at room temperature, beads from each sample were individually washed with 15 mL of buffer three times. For the elution of the different MBP-NepR/His-PhyR complexes, 100 μL of 20 mM Tris (pH 7.4) and 200 mM NaCl buffer, plus 10 mM maltose, was added to the beads. Fifteen microliters of each sample was loaded on a 14% SDS/PAGE gel, and spots corresponding to MBP-NepR and His-PhyR proteins were analyzed by ImageJ (National Institutes of Health) (41). The quantity of PhyR protein and mutant variants thereof was normalized to the amount of MBP-NepR on the gel. The same protocol was applied to study the binding of MBP-NepR to the His-PhyR$_{\Delta Rec}$(WT) and the His-PhyR$_{\Delta Rec}$(R15A-R16A) proteins.

The reciprocal copurification experiment was conducted by coexpressing the WT and His-PhyR$_{\Delta Rec}$ variants with NepR from pETDuet-1. Each complex was purified from a pellet from 50 mL of culture (*Protein Expression and Purification*). After nickel affinity immobilization with 100 μL of Ni^{2+} agarose resin and a 50-mL wash of each complex with 10 mM Tris (pH 7.4), 150 mM NaCl, and 10 mM imidazole buffer, each sample was eluted with 50 μL of 200 mM imidazole Tris·NaCl buffer and resolved by 14% SDS/PAGE gel for analysis (loading volume of 15 μL). Spots corresponding to NepR protein and to the different PhyR$_{\Delta Rec}$ proteins were analyzed by ImageJ. The quantity of NepR protein that was bound to affinity-immobilized PhyR-SL proteins was normalized to the amount of His-PhyR$_{\Delta Rec}$ on the gel. All copurification/pull-down experiments were conducted in triplicate.

SPR Binding Assays. The kinetics of WT and mutant PhyR binding to NepR were measured using a Bio-Rad ProteOn XPR six-channel SPR instrument. Preparation of the proteins for SPR assays was performed as follows: 50 mL of culture containing *E. coli* Rosetta (DE3) pLysS expressing either His-PhyR (WT or LΔ13 + Δα4) or His-PhyR$_{\Delta Rec}$ (WT or LΔ13 + Δα4) was grown (37 °C, 220 rpm) to an OD$_{660}$ of 0.5 and induced for 4 h with 1 mM IPTG. Pellets were resuspended in 1.5 mL of 50 mM Tris (pH 7.4), 150 mM NaCl, and 5 mM MgCl$_2$ buffer and disrupted two times by French press. After 10 min of centrifugation at 14,000 rpm, the supernatant was collected and filtered with a 0.22-μm filter (ThermoFisher Scientific). Each crude extract was diluted at a ratio of 1:4,000 and loaded onto a nitrilotriacetic acid Bio-Rad sensor chip and washed for 5 min with the previous buffer supplemented with 0.05% Tween 20.

MBP-NepR protein was purified by amylose affinity chromatography as described above. Different concentrations of MBP-NepR were tested to identify the ideal response range of the SPR chip, which was loaded with the different His-PhyR variants. Protein interaction between MBP-NepR and His-PhyR (WT or LΔ13 + Δα4) proteins was assayed under both phosphorylating conditions [using 50 mM Tris (pH 7.4), 150 mM NaCl, 5 mM MgCl$_2$, 5 mM AcP, and 0.05% Tween 20 buffer] and nonphosphorylating conditions [50 mM Tris (pH 7.4), 150 mM NaCl, 5 mM MgCl$_2$, and 0.05% Tween 20 buffer]. All protein dilutions were carried out in the buffer condition being tested.

As a control, we confirmed that the MBP tag alone is not able to interact with His-PhyR (WT or LΔ13 + Δα4) or His-PhyR$_{\Delta Rec}$ (WT or LΔ13 + Δα4) proteins, using the same protocol as above (Fig. S6 *E* and *F*).

PhyR/NepR and PhyR$_{\Delta Rec}$/NepR raw binding data were analyzed in the ProteOn software suite using the kinetic-Langmuir and the kinetic-heterogeneous ligand data analysis options, respectively. All SPR assays were conducted in triplicate.

MD Simulations. The crystal structure of full-length PhyR (PDB ID code 3N0R) was solvated in an aqueous KCl ionic solution to create a neutral system. A total of 49,493 atoms are in the model. After solvation, energy minimization was carried out in VMD (44) to remove any local strain and bad contacts. To prepare the system for MD, a predynamic equilibration of 1,000 steps was implemented to bring the system to a pressure of 1 bar and a temperature of 300 K. A simulation of 10 ns with the unphosphorylated protein was carried out to validate the methodology and ensure the stability of the system. A phosphate group was added to the structure on residue D192, and the phosphorylated protein was simulated for 320 ns. All simulations were carried out using the NAMD 2.7 b2 scalable MD software (42) with the all-atom CHARMM force field PARAM22 + CMAP (43). The temperature in the system was set to 300 K and maintained using Langevin dynamics on all nonhydrogen atoms; the damping coefficient was set to 0.5 ps^{-1}. The simulation was run with periodic boundary conditions. The particle mesh Ewald method was activated to calculate full system electrostatics at a grid point density of 1.5/Å. Pressure in the system was maintained with a Nosé–Hoover piston at every 200-fs window; the decay time scale was set to 100 fs. The trajectory was propagated with a multiple time-step scheme of 1 fs; bonded forces were evaluated at every step, nonbonded forces were evaluated every two steps, and long-range electrostatics were evaluated every four steps. The real-space, short-range electrostatics and van der Waals Lennard–Jones interactions were smoothly switched off in the interval from 10–12 Å. All calculations were preformed on the TeraGrid systems NCSA Abe and TACC Ranger. Images and trajectories were analyzed using VMD (44), PyMol (45), and RasMol (46). Original Tcl and MATLAB scripts were written for atomic distance calculations and contour maps.

Sequence Alignment and Protein Visualization Methods. Protein sequence alignments were carried out in Clustal W2 (www.ebi.ac.uk/clustalw/). PhyR ribbon structure rendering, electrostatic potential surfaces calculation (using the generate-vacuum electrostatics function), and visualization of the hydrophobic surfaces (according to the Eisenberg hydrophobicity scale (47) were performed with PyMOL. Visualization of the conserved residues in the different structures was performed using the Consurf server (48). PyMol and PDBe protein interfaces, surfaces, and assemblies (PISA) have been used to define the residue interaction map between NepR and PhyR$_{\Delta Rec}$(LΔ13).

ACKNOWLEDGMENTS. We thank Elena Solomaha (Chicago Biophysics Core) and Mohammed Yousef (Bio-Rad) for assistance with binding studies, and Jon Henry and Aretha Fiebig for technical advice and for criticism on a draft of this manuscript. S.C. acknowledges support for this project from National Institutes of Health Grant R01GM087353. B.R. acknowledges support from National Institutes of Health Grant R01CA093577. The Advanced Photon Source is supported by the Department of Energy Office of Basic Energy Sciences (Contract DE-AC02-06CH11357). The Life Sciences Collaborative Access Team is supported by the Michigan Economic Development Corporation and the Michigan Technology Tri-Corridor (Grant 085P1000817). The Biophysics Collaborative Access Team is a National Institutes of Health-supported research center (RR-08630). Computational resources were provided by the Teragrid through National Science Foundation Grant MCA01S018.

1. Gourion B, Rossignol M, Vorholt JA (2006) A proteomic study of Methylobacterium extorquens reveals a response regulator essential for epiphytic growth. *Proc Natl Acad Sci USA* 103:13186–13191.
2. Staroń A, Mascher T (2010) General stress response in α-proteobacteria: PhyR and beyond. *Mol Microbiol* 78:271–277.
3. Francez-Charlot A, et al. (2009) Sigma factor mimicry involved in regulation of general stress response. *Proc Natl Acad Sci USA* 106:3467–3472.
4. Staroń A, et al. (2009) The third pillar of bacterial signal transduction: Classification of the extracytoplasmic function (ECF) sigma factor protein family. *Mol Microbiol* 74:557–581.
5. Alvarez-Martinez CE, Lourenço RF, Baldini RL, Laub MT, Gomes SL (2007) The ECF sigma factor sigma(T) is involved in osmotic and oxidative stress responses in Caulobacter crescentus. *Mol Microbiol* 66:1240–1255.
6. Bastiat B, Sauviac L, Bruand C (2010) Dual control of Sinorhizobium meliloti RpoE2 sigma factor activity by two PhyR-type two-component response regulators. *J Bacteriol* 192:2255–2265.
7. Gourion B, et al. (2009) The PhyR-sigma(EcfG) signalling cascade is involved in stress response and symbiotic efficiency in Bradyrhizobium japonicum. *Mol Microbiol* 73: 291–305.
8. Price C (2002) General stress response. *Bacillus subtilis and Its Closest relatives: from Genes to Cells*, eds Sonenshein A, Hoch J, Losick R (ASM Press, Washington, DC), pp 369–384.
9. Alper S, Duncan L, Losick R (1994) An adenosine nucleotide switch controlling the activity of a cell type-specific transcription factor in B. subtilis. *Cell* 77:195–205.
10. Koonin E, Avarind L, Galperin M (2000) A comparative-genomic view of the microbial stress response. *Bacterial Stress Responses*, eds Storz G, Hengge-Aronis R (ASM Press, Washington, DC), pp 17–44.
11. Herrou J, Foreman R, Fiebig A, Crosson S (2010) A structural model of anti-anti-σ inhibition by a two-component receiver domain: The PhyR stress response regulator. *Mol Microbiol* 78:290–304.
12. Kaczmarczyk A, et al. (2011) Role of Sphingomonas sp. strain Fr1 PhyR-NepR-σEcfG cascade in general stress response and identification of a negative regulator of PhyR. *J Bacteriol* 193:6629–6638.
13. Lourenço RF, Kohler C, Gomes SL (2011) A two-component system, an anti-sigma factor and two paralogous ECF sigma factors are involved in the control of general stress response in Caulobacter crescentus. *Mol Microbiol* 80:1598–1612.
14. Lambert LJ, Wei Y, Schirf V, Demeler B, Werner MH (2004) T4 AsiA blocks DNA recognition by remodeling sigma70 region 4. *EMBO J* 23:2952–2962.

15. Thakur KG, Joshi AM, Gopal B (2007) Structural and biophysical studies on two promoter recognition domains of the extra-cytoplasmic function sigma factor sigma (C) from Mycobacterium tuberculosis. *J Biol Chem* 282:4711–4718.
16. Campbell EA, et al. (2003) Crystal structure of Escherichia coli sigmaE with the cytoplasmic domain of its anti-sigma RseA. *Mol Cell* 11:1067–1078.
17. Thakur KG, Praveena T, Gopal B (2010) Structural and biochemical bases for the redox sensitivity of Mycobacterium tuberculosis RslA. *J Mol Biol* 397:1199–1208.
18. Bellsolell L, Cronet P, Majolero M, Serrano L, Coll M (1996) The three-dimensional structure of two mutants of the signal transduction protein CheY suggest its molecular activation mechanism. *J Mol Biol* 257:116–128.
19. Birck C, et al. (1999) Conformational changes induced by phosphorylation of the FixJ receiver domain. *Structure* 7:1505–1515.
20. Bourret RB (2010) Receiver domain structure and function in response regulator proteins. *Curr Opin Microbiol* 13:142–149.
21. Varughese KI (2005) Conformational changes of Spo0F along the phosphotransfer pathway. *J Bacteriol* 187:8221–8227.
22. Solà M, et al. (2000) Towards understanding a molecular switch mechanism: Thermodynamic and crystallographic studies of the signal transduction protein CheY. *J Mol Biol* 303:213–225.
23. Tam C, Collinet B, Lau G, Raina S, Missiakas D (2002) Interaction of the conserved region 4.2 of sigma(E) with the RseA anti-sigma factor. *J Biol Chem* 277:27282–27287.
24. Anthony JR, Newman JD, Donohue TJ (2004) Interactions between the Rhodobacter sphaeroides ECF sigma factor, sigma(E), and its anti-sigma factor, ChrR. *J Mol Biol* 341: 345–360.
25. Campbell EA, Westblade LF, Darst SA (2008) Regulation of bacterial RNA polymerase sigma factor activity: A structural perspective. *Curr Opin Microbiol* 11:121–127.
26. Campbell EA, et al. (2007) A conserved structural module regulates transcriptional responses to diverse stress signals in bacteria. *Mol Cell* 27:793–805.
27. Murakami KS, Masuda S, Campbell EA, Muzzin O, Darst SA (2002) Structural basis of transcription initiation: An RNA polymerase holoenzyme-DNA complex. *Science* 296: 1285–1290.
28. Murakami KS, Masuda S, Darst SA (2002) Structural basis of transcription initiation: RNA polymerase holoenzyme at 4 A resolution. *Science* 296:1280–1284.
29. Vassylyev DG, et al. (2002) Crystal structure of a bacterial RNA polymerase holoenzyme at 2.6 A resolution. *Nature* 417:712–719.
30. Teng TY (1990) Mounting of crystals for macromolecular crystallography in a freestanding thin-film. *J Appl Cryst* 23:387–391.
31. Doublié S (2007) Production of selenomethionyl proteins in prokaryotic and eukaryotic expression systems. *Methods Mol Biol* 363:91–108.
32. Otwinowski Z, Minor W (1997) Processing of X-ray diffraction data collected in oscillation mode. *Macromolecular Crystallography Part A* 276:307–326.
33. Strong M, et al. (2006) Toward the structural genomics of complexes: Crystal structure of a PE/PPE protein complex from *Mycobacterium tuberculosis*. *Proc Natl Acad Sci USA* 103:8060–8065.
34. Dauter Z (2002) One-and-a-half wavelength approach. *Acta Crystallogr D Biol Crystallogr* 58:1958–1967.
35. Adams PD, et al. (2010) PHENIX: A comprehensive Python-based system for macromolecular structure solution. *Acta Crystallogr D Biol Crystallogr* 66:213–221.
36. Emsley P, Lohkamp B, Scott WG, Cowtan K (2010) Features and development of Coot. *Acta Crystallogr D Biol Crystallogr* 66:486–501.
37. Ried JL, Collmer A (1987) An *nptI-sacB-sacR* cartridge for constructing directed, unmarked mutations in gram-negative bacteria by marker exchange-eviction mutagenesis. *Gene* 57:239–246.
38. Fiebig A, Castro Rojas CM, Siegal-Gaskins D, Crosson S (2010) Interaction specificity, toxicity and regulation of a paralogous set of ParE/RelE-family toxin-antitoxin systems. *Mol Microbiol* 77:236–251.
39. Miller JH (1972) *Experiments in Molecular Genetics* (Cold Spring Harbor Laboratory Press, Plainview, NY), pp 352–355.
40. Thanbichler M, Iniesta AA, Shapiro L (2007) A comprehensive set of plasmids for vanillate- and xylose-inducible gene expression in Caulobacter crescentus. *Nucleic Acids Res* 35:e137.
41. Abramoff MD, Magelhaes PJ, Ram SJ (2004) Image processing with ImageJ. *Biophotonics International* 11:36–42.
42. Phillips JC, et al. (2005) Scalable molecular dynamics with NAMD. *J Comput Chem* 26: 1781–1802.
43. Brooks BR, et al. (2009) CHARMM: The biomolecular simulation program. *J Comput Chem* 30:1545–1614.
44. Humphrey W, Dalke A, Schulten K (1996) VMD: Visual molecular dynamics. *J Mol Graph* 14:33–38, 27–28.
45. Schrödinger LLC (2010) The PyMol Molecular Graphics System (Schrödinger LLC, Portland, OR), Version 1.3.
46. Sayle RA, Milner-White EJ (1995) RASMOL: Biomolecular graphics for all. *Trends Biochem Sci* 20:374.
47. Eisenberg DSE, Komarony M, Wall R (1984) Amino acid scale: Normalized consensus hydrophobicity scale. *J Mol Biol* 179:125–142.
48. Ashkenazy H, Erez E, Martz E, Pupko T, Ben-Tal N (2010) ConSurf 2010: Calculating evolutionary conservation in sequence and structure of proteins and nucleic acids. *Nucleic Acids Res* 38(Web Server issue):W529–W533.

Supporting Information

Herrou et al. 10.1073/pnas.1116887109

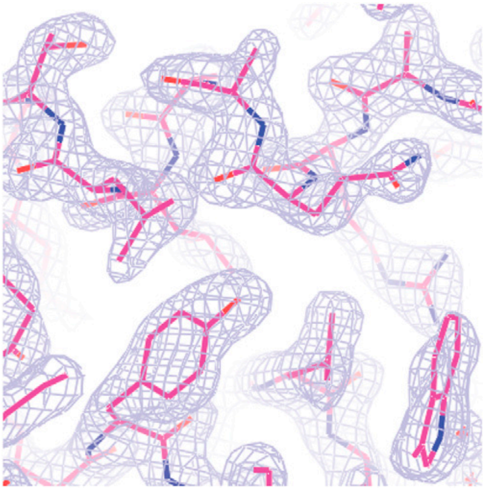

Fig. S1. Simulated annealing composite omit map of a region of the PhyR$_{\Delta Rec}$(LΔ13)/NepR complex (contoured at 1.5 σ).

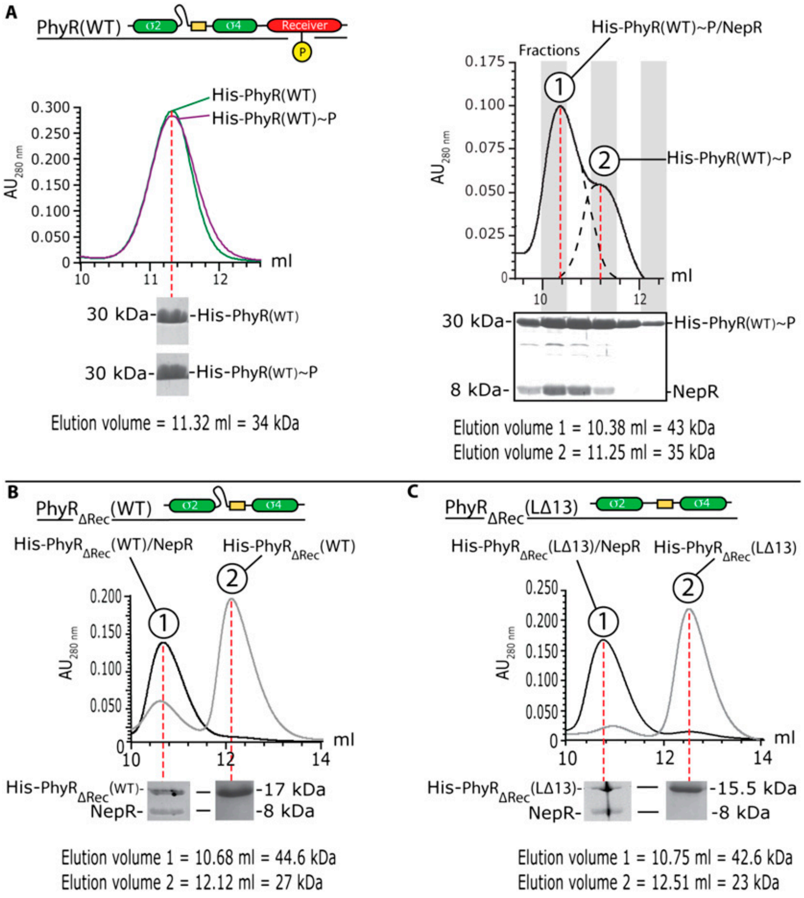

Fig. S2. Size exclusion chromatography. Elution volumes and corresponding molecular weights are labeled. (*A*) (*Left*) Elution profile of His-PhyR(WT) under non-phosphorylating conditions (green) or phosphorylating (Mg^{2+}, AcP) conditions (purple curve). (*Right*) Elution profile of His-PhyR(WT) coexpressed in pETDuet-1 with NepR and purified in presence of Mg^{2+} and AcP. (*B*) Elution profile of His-PhyR$_{\Delta Rec}$(WT)/NepR complex (black curve) and His-PhyR$_{\Delta Rec}$(WT) alone (gray curve). (*C*) Elution profile of the His-PhyR$_{\Delta Rec}$(LΔ13)/NepR complex (black curve) and the purified His-PhyR$_{\Delta Rec}$(LΔ13) alone (gray curve). AU$_{280\ nm}$, absorbance units at 280 nanometers.

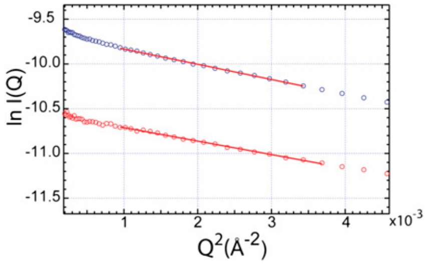

Fig. S3. Guinier analysis of SAXS data from His-PhyR(WT) in the presence and absence of Mg^{2+} and AcP. The concentration of PhyR collected under nonphosphorylating conditions (i.e., in the absence of AcP and Mg^{2+}) was ~20 μM (blue open circles), and the sample under phosphorylating conditions was ~8 μM (red open circles). Fitted plots (Q_{max}·R_g = 1.3) of protein solution under nonphosphorylating and phosphorylating conditions yielded R_g values of 22.5 ± 0.2 Å and 21.3 ± 0.4 Å, respectively. ln I(Q), where I(Q) is intensity as a function of the scattering vector, Q.

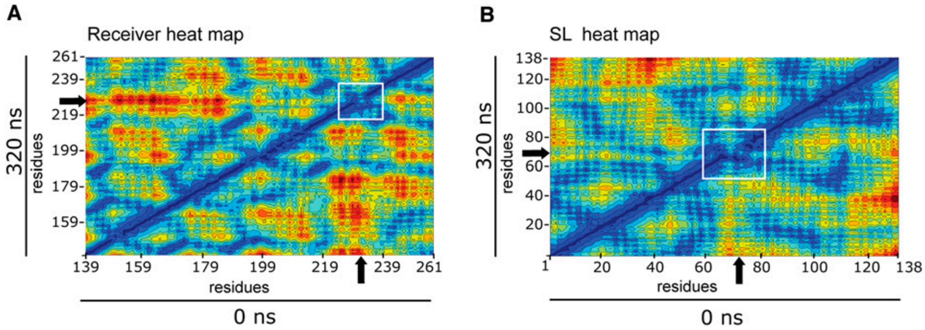

Fig. S4. All-atom MD simulation of PhyR~P. (*A*) Heat map illustration of residue (defined by center of mass) movement relative to all residue positions between 0 and 320 ns (dark blue, 0–5 Å movement; light blue, 5–10 Å; ranging to red, >30 Å; binned in 5 Å intervals). The α11-β5 region of the receiver structure is marked with black arrows and highlighted in a white box. (*B*) Heat map illustration of residue movement relative to all residue positions between 0 and 320 ns colored as in *A*. The α3-α4 region of PhyR-SL of the structure is marked with black arrows and highlighted in a white box.

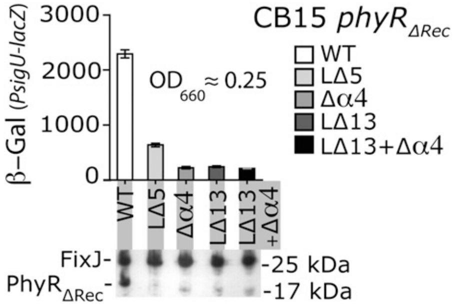

Fig. S5. P*sigU-lacZ* transcription in *C. crescentus* expressing PhyR in which the receiver domain has been entirely deleted (PhyR$_{\Delta Rec}$). Transcription was assayed in WT PhyR$_{\Delta Rec}$ (WT) and in strains encoding PhyR$_{\Delta Rec}$ proteins carrying the LΔ5, LΔ13, LΔ13 + α4, and α4 deletions as detailed in Fig. 6*B*. In vivo stability of proteins as determined by Western blot analysis is shown below the bar graph; FixJ is the loading control.

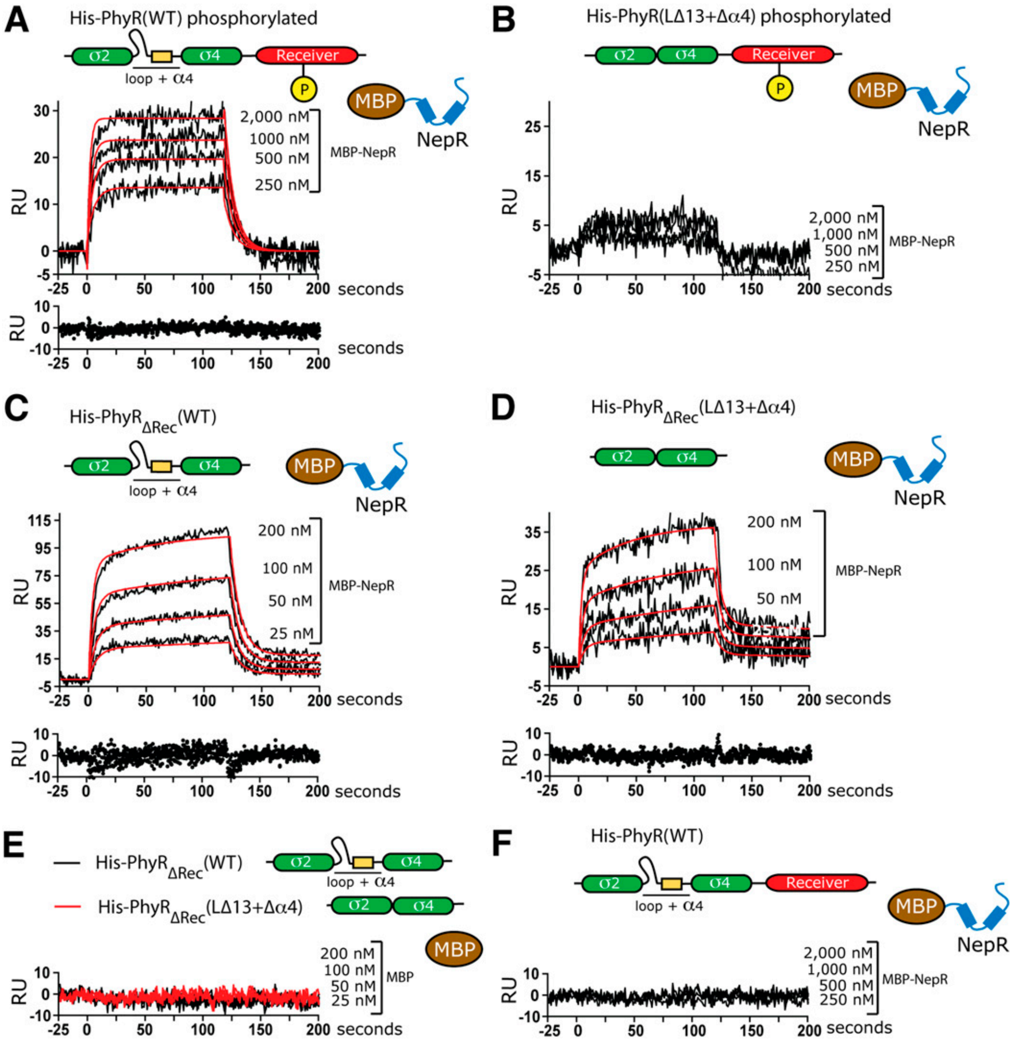

Fig. S6. SPR sensorgrams from PhyR/NepR binding experiments. Binding data are fitted in red, and residuals are shown below the sensorgrams. (*A*) Binding assessed between His-PhyR(WT) and MBP-NepR at 2,000, 1,000, 500, and 250 nM (black).The experiment was carried out in the presence of AcP (5 mM) and MgCl$_2$ (5 mM) in the flow buffer. (*B*) Binding assessed between His-PhyR(LΔ13 + Δα4) and MBP-NepR; the experiment carried out under equivalent conditions as in *A*. (*C*) Binding assessed between His-PhyR$_{\Delta Rec}$(WT) and MBP-NepR (at 200, 100, 50, and 25 nM) in the absence of AcP and Mg^{2+}. (*D*) Binding assessed between His-PhyR$_{\Delta Rec}$(LΔ13 + Δα4) and MBP-NepR under the same conditions as in *C*. (*E*) Control experiment in which binding was assessed between His-PhyR$_{\Delta Rec}$(WT) (black) or His-PhyR$_{\Delta Rec}$(LΔ13 + Δα4) (red) and MBP analyte at 200, 100, 50, and 25 nM. (*F*) Control experiment in which binding was assessed between the His-PhyR(WT) and MBP-NepR (at 2,000, 1,000, 500 and 250 nM) in the absence of AcP and Mg^{2+} in the flow buffer. RU, resonance units.

Table S1. Primers

Names	Sequences	Restriction sites	Notes
PhyR1-UP	5′ gaattctcacgcttgaagctgttgtc 3′	EcoRI	Used for *phyR* cloning in pNPTS138 suicide vector
PhyR1-LO	5′ GCATGCctatgacatgcgcttcc 3′	SphI	
PhyR2-UP	5′ GGATCCAatgagtcttcttgctcgcttggc 3′	BamHI	Used to amplify *phyR* for pETDuet-1 (position 1)
PhyR2-LO	5′ AAGCTTtcaggccgccttagcggt 3′	HindIII	
PhyR2-UP	See sequence in this table	BamHI	Used to amplify *phyR-SL* for pETDuet-1 (position 1)
PhyR-SL-LO	5′ AAGCTTtcaggtcgccagctcgg 3′	HindIII	
PhyR3-UP	5′ CATATGAGTCTTCTTGCTCGCTTGGC 3′	NdeI	Used to amplify *phyR* for pET28c
PhyR2-LO	See sequence in this table	HindIII	
PhyR3-UP	See sequence in this table	NdeI	Used to amplify *phyR-SL* for pET28c
PhyR-SL-LO	See sequence in this table	HindIII	
R15A-R16A-UP	5′ CTTACATCgcCgcCTACGCCC 3′		Used to mutate R15 and R16 to Ala in PhyR-SL
R15A-R16A-LO	5′ GGGCGTAGgcGgcGATGTAAG 3′		
LΔ13 + Δα4-UP	5′ agctccggggcccaaatcgcgccgcgctcg 3′	—	Used for ΔL71R91 deletion corresponding to the loop and α4
LΔ13 + Δα4-LO	5′ ttgggccccggagctgag 3′	—	
LΔ5-UP	5′ gctcagctccggggcccacgaccagggcctgcacg 3′	—	Used for ΔQ70G74 deletion corresponding to 5 amino acids of the loop
LΔ5-LO	5′ ggccccggagctgagcc 3′	—	
LΔ13-UP	5′ atctggctcagctccgccggcgacgacgcc 3′	—	Used for ΔG68H80 deletion corresponding to 13 amino acids of the loop
LΔ13-LO	5′ ggagctgagccagatggcgtg 3′	—	
Δα4-UP	5′ gcacgccggcgacgcgccgcgctcgcgt 3′	—	Used for ΔD84I92 deletion corresponding to α4
Δα4-LO	5′ gtcgccggcgtgcagg 3′	—	
ΔRec-UP	5′ CCGAGCTGGCGACCTGAGAGCCCTAAGAC 3′	—	Used for ΔE142A266 deletion corresponding to the PhyR receiver domain
ΔRec-LO	5′ GTCTTAGGGCTCTCAggtcgccagctcgg 3′	— —	
NepR1-UP	5′ CATatgaacttcggcgtcgaggac 3′	NdeI	Used to amplify *nepR* for pETDuet-1 (position 2)
NepR1-LO	5′ CCTAGGctactcgccccccgcc 3′	AvRII	
NepR2-UP	5′ GAATTCATGaacttcggcgtcgaggac 3′	EcoRI	Used to amplify *nepR* for pMAL-c2g
NepR2-LO	5′ AAGCTTctactcgccccccgcc 3′	HindIII	
PsigU-UP	5′ GAATTCAAGGCCGCGTTCAGGTC 3′	EcoRI	Used to amplify the promoter region of *sigU* for pRKLac290
PsigU-LO	5′ CTGCAGTCTGAGTCTGCTGGTCCATCT 3′	XhoI	
pXyl-UP	5′ TAAGCACTTGGGTGAGAAGCCC 3′	—	Used to introduce an HA epitope before the MCS of pMT585
GFP-LO	5′ ggtgcgctcctggacgt 3′	—	
HA-UP	5′ cgacgtcccggactacgcccatatgcctgcaggcgcctta 3′	—	
HA-LO	5′ tccgggacgtcgtacgggtacatatAgtcgtctccccaaa 3′	—	

Table S2. **Strains**

Strains	Genotype	Deletions/mutations	Genes	Source	Notes
FC3	*E. coli MT607/pRK600*	—	—	(1)	Helper strain used for mating between FC799 and Top10 pNPTS138-*phyr* and *phyR*$_{\Delta Rec}$ variants; also used to introduce pRKLac290-P*sigU* into the different CB15 strains
FC799	CB15 Δ*phyR*	ΔA8G252	CC_3477	(2)	*Caulobacter* strain in which the *phyR* gene is deleted, used as acceptor strain for allelic exchange
FC634	Top10/pRKLac290-P*sigU*	—	CC_2883	This study	Strain carrying *lacZ* in transcriptional fusion with the *sigU* promoter
FC1494	CB15 *phyR(WT)*/pRKLac290-P*sigU*	—	CC_3477	This study	*Caulobacter phyR* variant strains; used to measure β-gal activities under sucrose stress conditions
FC1497	CB15 *phyR(LΔ13 + Δα4)*/pRKLac290-P*sigU*	ΔL71R91	CC_3477	This study	
FC1500	CB15 *phyR(LΔ5)*/pRKLac290-P*sigU*	ΔQ70G74	CC_3477	This study	
FC1503	CB15 *phyR(LΔ13)*/pRKLac290-P*sigU*	ΔG68H80	CC_3477	This study	
FC1506	CB15 *phyR(Δα4)*/pRKLac290-P*sigU*	ΔD84I92	CC_3477	This study	
FC1509	CB15 *phyR*$_{\Delta Rec}$*(WT)*/pRKLac290-P*sigU*	ΔE142A266	CC_3477	This study	*Caulobacter phyR*$_{\Delta Rec}$ variant strains; used to measure β-gal activities under sucrose stress conditions
FC1512	CB15 *phyR*$_{\Delta Rec}$*(LΔ13 + Δα4)*/pRKLac290-P*sigU*	ΔL71R91/ΔE142A266	CC_3477	This study	
FC1515	CB15 *phyR*$_{\Delta Rec}$*(LΔ5)*/pRKLac290-P*sigU*	ΔQ70G74/ΔE142A266	CC_3477	This study	
FC1518	CB15 *phyR*$_{\Delta Rec}$*(LΔ13)*/pRKLac290-P*sigU*	ΔG68H80/ΔE142A266	CC_3477	This study	
FC1521	CB15 *phyR*$_{\Delta Rec}$*(Δα4)*/pRKLac290-P*sigU*	ΔD84I92/ΔE142A266	CC_3477	This study	
FC1522	Rosetta (DE3) pLysS/pMAL2cg	—	—	This study	Used for MBP overexpression
FC1524	Rosetta (DE3) pLysS/pMAL2cg-*nepR*	—	CC_3476	This study	Used for MBP-NepR overexpression
FC1527	Rosetta (DE3) pLysS/pETDuet-1 *His-phyR*$_{\Delta Rec}$*(WT) + nepR*	ΔE142A266	CC_3476 CC_3477	This study	Used for overexpression of His tagged WT and mutant PhyR-SL in complex with NepR
FC1529	Rosetta (DE3) pLysS/pETDuet-1 *His-phyR*$_{\Delta Rec}$*(LΔ13 + Δα4) + nepR*	ΔL71R91/ΔE142A266	CC_3476 CC_3477	This study	
FC1531	Rosetta (DE3) pLysS/pETDuet-1 *His-phyR*$_{\Delta Rec}$*(LΔ5) + nepR*	ΔQ70G74/ΔE142A266	CC_3476 CC_3477	This study	
FC1533	Rosetta (DE3) pLysS/pETDuet-1 *His-phyR*$_{\Delta Rec}$ *(LΔ13) + nepR*	ΔG68H80/ΔE142A266	CC_3476 CC_3477	This study	
FC1535	Rosetta (DE3) pLysS/pETDuet-1 *His-phyR*$_{\Delta Rec}$*(Δα4) + nepR*	ΔD84I92/ΔE142A266	CC_3476 CC_3477	This study	
FC1536	Rosetta (DE3) pLysS/pET28c *His-phyR(WT)*	—	CC_3477	This study	Used for overexpression of His tagged WT and mutant PhyR
FC1538	Rosetta (DE3) pLysS/pET28c *His-phyR(LΔ13 + Δα4)*	ΔL71R91	CC_3477	This study	
FC1540	Rosetta (DE3) pLysS/pET28c *His-phyR(LΔ5)*	ΔQ70G74	CC_3477	This study	
FC1542	Rosetta (DE3) pLysS/pET28c *His-phyR(LΔ13)*	ΔG68H80	CC_3477	This study	
FC1544	Rosetta (DE3) pLysS/pET28c *His-phyR(Δα4)*	ΔD84I92	CC_3477	This study	
FC1546	Rosetta (DE3) pLysS/pET28c *His-phyR*$_{\Delta Rec}$*(WT)*	ΔE142A266	CC_3477	This study	Used for overexpression of His tagged WT and mutant PhyR-SL
FC1548	Rosetta (DE3) pLysS/pET28c *His-phyR*$_{\Delta Rec}$*(LΔ13 + Δα4)*	ΔL71R91/ΔE142A266	CC_3477	This study	

Table S2. Cont.

Strains	Genotype	Deletions/mutations	Genes	Source	Notes
FC1556	Rosetta (DE3) pLysS/pETDuet-1 *His-phyR(WT) + nepR*	—	CC_3476 CC_3477	This study	Used for overexpression of His tagged WT PhyR in complex with NepR
FC1557	*E. coli* Top10/pMT585-HA	—	—	This study	Strain carrying a Xylose inducible pMT585 vector with an HA tag engineered in the multicloning site
FC1559	CB15 Δ*phyR* xylX::pMT585-HA-*phyR(WT)*	—	CC_3477	This study	Used for overexpression of HA-tagged PhyR variants in CB15 (for Western blot)
FC1561	CB15 Δ*phyR* xylX::pMT585-HA-*phyR(L*Δ*13 +* Δα*4)*	ΔL71R91	CC_3477	This study	
FC1563	CB15 Δ*phyR* xylX::pMT585-HA-*phyR(L*Δ*5)*	ΔQ70G74	CC_3477	This study	
FC1565	CB15 Δ*phyR* xylX::pMT585-HA-*phyR(L*Δ*13)*	ΔG68H80	CC_3477	This study	
FC1567	CB15 Δ*phyR* xylX::pMT585-HA-*phyR(*Δα*4)*	ΔD84I92	CC_3477	This study	
FC1569	CB15 Δ*phyR* xylX::pMT585-HA-*phyR*$_{\Delta Rec}$*(WT)*	ΔE142A266	CC_3477	This study	Used for overexpression of HA-tagged PhyR-SL variants in CB15 (for Western blot)
FC1571	CB15 Δ*phyR* xylX::pMT585-HA-*phyR*$_{\Delta Rec}$*(L*Δ*13 +* Δα*4)*	ΔL71R91/ΔE142A266	CC_3477	This study	
FC1573	CB15 Δ*phyR* xylX::pMT585-HA-*phyR*$_{\Delta Rec}$*(L*Δ*5)*	ΔQ70G74/ΔE142A266	CC_3477	This study	
FC1575	CB15 Δ*phyR* xylX::pMT585-HA-*phyR*$_{\Delta Rec}$*(L*Δ*13)*	ΔG68H80/ΔE142A266	CC_3477	This study	
FC1577	CB15 Δ*phyR* xylX::pMT585-HA-*phyR*$_{\Delta Rec}$*(*Δα*4)*	ΔD84I92/ΔE142A266	CC_3477	This study	
FC1766	Rosetta (DE3) pLysS/pET28c *His-phyR*$_{\Delta Rec}$*(R15A-R16A)*	R15A-R16A	CC_3477	This study	Used for overexpression of His-tagged PhyR-SL (R15A-R16A)
FC1769	CB15 *phyR(R15A-R16A)*/ pRKLac290-P*sigU*	R15A-R16A	CC_3477	This study	*Caulobacter phyR* and *phyR*$_{\Delta Rec}$ (R15A-R16A) strains; used to measure β-gal activities under sucrose stress conditions
FC1772	CB15 *phyR*$_{\Delta Rec}$*(R15A-R16A)*/ pRKLac290-P*sigU*	R15A-R16A	CC_3477	This study	
FC1774	CB15 Δ*phyR* xylX::pMT585-HA-*phyR(R15A-R16A)*	R15A-R16A	CC_3477	This study	Used for overexpression of HA-tagged PhyR and PhyR-SL (R15A-R16A) variants in CB15 (for Western blot)
FC1776	CB15 Δ*phyR* xylX::pMT585-HA-*phyR*$_{\Delta Rec}$*(R15A-R16A)*	R15A-R16A	CC_3477	This study	

1. Fiebig A, Castro Rojas CM, Siegal-Gaskins D, Crosson S (2010) Interaction specificity, toxicity and regulation of a paralogous set of ParE/RelE-family toxin-antitoxin systems. *Mol Microbiol* 77:236–251.
2. Herrou J, Foreman R, Fiebig A, Crosson S (2010) A structural model of anti-anti-σ inhibition by a two-component receiver domain: The PhyR stress response regulator. *Mol Microbiol* 78:290–304.

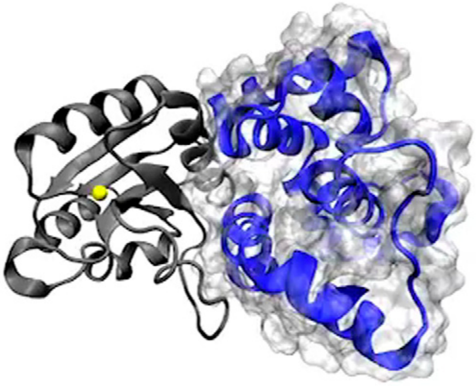

Movie S1. Trajectory of the MD simulation of PhyR~P from 0–320 ns is shown. Each frame shows 5 ns of simulation time. The phosphorous atom at the phosphorylation site is shown in yellow as a bead. The SL domain of PhyR is shown in blue with the surface rendered as a transparency. The receiver domain is shown in silver.

Movie S1